ADVANCED FUNCTIONAL MATERIALS
www.afm-journal.de

Streamlined Synthesis of Ga-Cu Dual Single-Atom Nanozymes for Advanced Electrochemical Sensing Applications

*Guangchun Song, Xiaochun Zheng, Zedong Zhang, Marie-Laure Fauconnier, Cheng Li, Li Chen, and Dequan Zhang**

The real-time, rapid, and portable detection of food freshness is crucial for assessing food quality and ensuring food safety. Volatile amines produced during food spoilage have significant potential as markers for evaluating freshness. In this study, an electrochemical sensing platform is developed for the detection of volatile amines using gallium-copper dual single-atom nanozymes (with Ga and Cu contents of 1.31and 4.07 wt.%, respectively) supported by a 2D layered double hydroxide (LDH). The synergistic loading of the dual atoms facilitated binding with volatile amines, which accelerated electron transfer at the GaCu-LDH surface, inducing changes in the electrical signals and enabling detection. The platform exhibited a rapid response time of ≈4 s, with a good linear relationship between the ammonia concentration and steady-state current within the range of 0.05–0.4 mM and a detection limit of 5.9 µM. This electrochemical sensor platform enabled the rapid, portable, and intelligent detection and monitoring of the freshness of meat from livestock and poultry (pork, beef, lamb, and chicken) at room temperature and under refrigerated storage conditions, providing a valuable method for the real-time monitoring of food freshness.

1. Introduction

Food freshness is essential to consumer health and safety. According to a report by the World Health Organization, ≈600 million cases of illness worldwide are caused by the consumption of spoiled food products,[1–3] with over 200 diseases linked to food spoilage.[4] With the faster pace of modern lifestyles, there has been a surge in the demand for meat, a primary source of high-quality protein. Hence, ensuring the quality and safety of meat products has emerged as a key research focus.[5] During processing, storage, and distribution, meat is prone to quality deterioration owing to lipid oxidation,[6,7] protein oxidation and degradation,[6,8] and microbial spoilage.[9,10] In the European Union, ≈14 million tons are meat is wasted annually owing to delays in spoilage detection,[11] while resource losses in China are significantly higher than the 1–3% in developed countries.[11,12] Therefore, the development of rapid, portable, and intelligent technologies for the precise detection and monitoring of meat freshness is crucial for reducing economic losses, ensuring public health, and promoting efficient resource use.

The total volatile basic nitrogen (TVB-N) is currently recognized as the sole physicochemical indicator for evaluating meat freshness. However, the detection process is cumbersome and does not meet the demands for on-site, rapid, and portable detection.[13–15] Therefore, the development of a fast and portable technology for detecting meat freshness is imperative. Nitrogen-containing organic compounds produced by the decarboxylation and degradation of amino acids, peptides, and proteins under microbial activity during meat spoilage are potential markers for evaluating meat freshness.[16–18] Volatile amines are particularly noteworthy as potential markers for the following reasons:[19–22] 1) changes in their concentration reflect the extent of protein oxidation in meat and are significantly correlated with the TVB-N content; 2) the unpleasant odors of volatile amines provide a direct sensory indication of meat spoilage; 3) volatile amines can be detected using relatively simple chemical analysis methods. Hence, volatile amines can serve as effective markers for the development of rapid, portable, and intelligent technologies for determining meat freshness.

Traditional large-scale detection methods, such as chromatography-mass spectrometry[20,23] and spectroscopy,[24,25] can detect volatile amines; however, their application in rapid,

G. Song, X. Zheng, C. Li, L. Chen, D. Zhang
Institute of Food Science and Technology
Chinese Academy of Agricultural Sciences, Key Laboratory of Agro-products Quality and Safety Control in Storage and Transport Process
Ministry of Agriculture and Rural Affairs
Beijing 100193, China
E-mail: dequan_zhang0118@126.com
G. Song, M.-L. Fauconnier
Laboratory of Chemistry of Natural Molecules
Gembloux Agro-Bio Tech
University of Liege
Passage des déportés 2, Gembloux B-5030, Belgium
Z. Zhang
Department of Chemistry
Tsinghua University
Beijing 100084, China

The ORCID identification number(s) for the author(s) of this article can be found under https://doi.org/10.1002/adfm.202510909

DOI: 10.1002/adfm.202510909

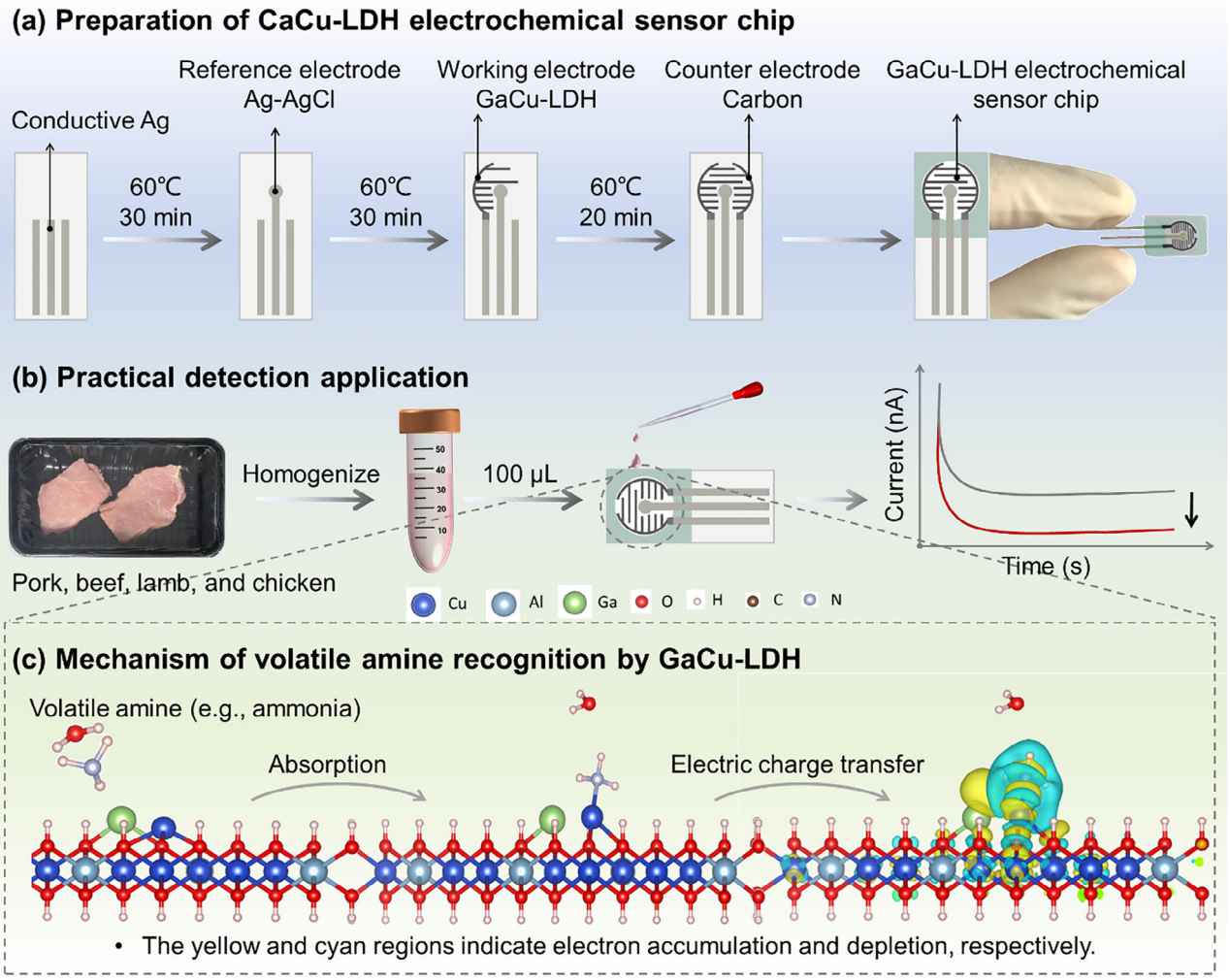

Scheme 1. Preparation and practical detection application of a GaCu-LDH electrochemical sensing chip.

portable, and intelligent sensing is limited owing to high costs and the need for professional operation.[26–29] Materials are often regarded as the "cornerstone of human civilization," and the development and application of novel high-performance nanomaterials have been a major focus of interdisciplinary research.[30] In this context, single-atom nanozymes (SAzymes) have attracted significant attention because of their uniformly distributed catalytically active centers, well-defined electronic structures, and precisely designed geometric configurations. SAzymes also possess other desirable properties such as strong optical signals and ease of modification, making them highly promising for rapid, portable, and intelligent sensing applications.[31,32] Many studies have shown that the catalytic performance of enzymes can be effectively regulated by adjusting the type of carrier and number of catalytic metal centers.[33–36] 2D layered double hydroxides (LDHs) composed of positively charged metal hydroxide layers and negatively charged interlayer anions have emerged as a novel class of functional nanomaterials.[37–39] Owing to their unique 2D layered structure, simple preparation, high surface area, and superior catalytic activity, LDHs offer distinct advantages over carbon-based and metal-organic framework materials when used as carriers for SAzymes.[40–42] Increasing the number of metal atoms in coordination with single-atom metal catalysts is an effective strategy for enhancing the catalytic activity and stability of SAzymes.[43–46]

The synergistic catalysis of LDHs and dual SAzymes allows metal atoms to be loaded onto LDHs to form layered structures not only with nonmetal atoms but also with surrounding metal atoms. This creates a complex and flexible environment in which the catalytic efficiency of SAzymes can be precisely regulated. The incorporation of dual atoms overcomes the limitations of single-atom catalysts, such as low catalytic activity, poor stability, limited selectivity, and a narrow range of reactions. Hence, this study focuses on harnessing the superior properties of LDHs as a carrier material. By incorporating two metal atoms in the synthesis of novel dual SAzymes, enhanced catalytic performance, strong stability, and high selectivity are achieved, specifically in the detection of volatile amines (**Scheme 1**). Furthermore, a portable electrochemical detection sensor is developed based on this material, providing a new platform for the rapid, portable, and intelligent

detection of meat freshness. This approach not only advances the practical application of the materials but also offers effective solutions for their use in real-life scenarios.

2. Results and Discussion

2.1. Synthesis and Characterization of GaCu-LDH, Ga-LDH, Cu-LDH, and LDH

Based on the authors' previous research,[47] Ga and Cu SAzymes exhibit stronger enzyme-like catalytic performance than single-atom nanocatalysts employing other metals (Mn and Zn). Therefore, the further exploration of the unique enzyme-like catalytic performance of dual-coordinated Ga and Cu is of significance. Using LDHs as the carrier material, GaCu-LDH, Ga-LDH, Cu-LDH, and LDH were synthesized via coprecipitation. The morphologies and elemental compositions of the four LDH materials were characterized using transmission electron microscopy (TEM), energy-dispersive X-ray spectrometry (EDS), high-angle annular dark-field scanning transmission electron microscopy (HAADF-STEM), selected-area electron diffraction (SAED), electron energy loss spectroscopy (EELS), X-ray photoelectron spectroscopy (XPS), and X-ray diffraction (XRD). GaCu-LDH, Ga-LDH, Cu-LDH, and LDH exhibited irregular layered sheet morphologies (**Figure 1**a,b; Figures S1a,b and S2a,b, and S3, Supporting Information). Ga, Cu, and Al were detected in GaCu-LDH (Figure 1c; Figures S1c–e, S2c–e, S4, Supporting Information), whereas Ga, Cu, and Al were present in Ga-LDH (Figure S1c–e, Supporting Information), and Cu and Al were detected in Cu-LDH (Figure S2c–e, Supporting Information). HAADF-STEM analysis revealed that the isolated single-atom metals were evenly dispersed within the layered framework (Figure 1d). Further SAED analysis showed a characteristic interlayer spacing of ≈0.25 nm (Figure 1e). This observation is consistent with the XRD analysis, confirming the (012) and (110) lattice planes and demonstrating that lattice tuning and a balance with structural stability are achieved through dual doping (Figure 1f; Figure S5, Supporting Information). Based on a comparison with the JCPDS card, the peaks in the range of 25–30° for Ga-LDH and Cu-LDH originated from a secondary phase, for which the corresponding standard card number is 83–1506 (Figure S5, Supporting Information). Complementary EELS elemental mapping showed the co-localization of Ga, Cu, and Al in the layered framework, with distinct energy-loss edges, providing firm evidence of the coexistence of Ga and Cu single-atom metal centers (Figure S6, Supporting Information). Notably, the detected signal of Al metal originated from the hydrotalcite support and did not interfere with the verification of the GaCu dual single-atom configuration.

Further, comprehensive XPS analysis indicated that Ga^{3+} ($3d_5/_2$ = 18.9 eV, $3d_3/_2$ = 21.2 eV) in the GaCu-LDH material predominantly occupies the octahedral [GaO_6] sites in the brucite-like layers, bonded via strong covalent interactions. The binding-energy shift (Δ = −0.3 eV) and XRD lattice contraction (Δc = −1.8%) together confirm the enhanced rigidity of the brucite layers (Figure S7, Supporting Information). Trace amounts of Ga^0 ($3d_5/_2$ = 16.5 eV, 9.8% relative abundance) were present in the form of sub-nanometer clusters, where Ga may plausibly optimize the electronic structure of the Cu^{2+} active centers via d-band modulation (d-band center = −2.3 eV) (Figure 1g). The Cu 2p spectrum shows typical Cu^{2+} splitting peaks at 934.6 eV ($2p_3/_2$) and 954.3 eV ($2p_1/_2$), accompanied by a strong satellite peak at 943.1 eV (Sat.), ruling out the presence of Cu^0 or Cu^+ species. The significant shift in the binding energy relative to that of the CuO reference (+1.1 eV) confirms that Cu^{2+} was stabilized on the LDH layers through strong coordination with the interlayer anions. Combined with the Auger parameter (α = 1851.2 eV) and HAADF-STEM data, the results confirm the single-atom dispersion of Cu^{2+} (Figure 1h). The Al 2p spectrum shows a main peak at 74.8 eV, corresponding to the 2p orbital of Al^{3+}, which is consistent with the [AlO_6] unit in the hydrotalcite structure; the secondary peak at 77.2 eV is attributed to the Cu^{2+} $3p_3/_2$ signal. This depth-sensitive signal confirms the 3D, uniform distribution of the Cu species within the brucite layers (Figure 1i), which collaboratively maintain the stability of the layers. In the dual single-atom structure, Ga^{3+} and Cu^{2+} achieve cooperative charge regulation through bridging M-O-M (Ga-O-Cu) bonds, whereas Al^{3+} acts as a structural stabilizer, maintaining the integrity of the layered framework. The synergistic electronic states of the three elements provide a critical structural foundation for enhancing the redox activity of GaCu-LDH. Similar results were obtained for the other three materials (Figures S8–S10, Supporting Information).

The metal contents of the four materials were measured using inductively-coupled plasma mass spectrometry (ICP-MS), which revealed that GaCu-LDH contained 1.31 wt.% Ga and 4.07 wt.% Cu (Table S1, Supporting Information). These values represent the single-atom metal contents of Ga and Cu in GaCu-LDH. In addition, Ga-LDH contained 2.41 wt.% Ga and Cu-LDH contained 3.27 wt.% Cu. These findings indicate that the dual-atom content is comparable to that of single-metal atoms, demonstrating the uniform distribution of metal atoms during synthesis and further confirming the reliability of the synthesis method. Additionally, the metal content of GaCu-LDH was relatively higher than that of other dual SAzymes (Table S1, Supporting Information).

The coordination environment and chemical valence state of GaCu-LDH were investigated using the X-ray absorption fine structure (XAFS) technique. X-ray absorption near-edge structure (XANES) analysis indicated that the valence state of Ga is 3+ (**Figure 2**a), while that of Cu is close to 2+ (Figure 2b), consistent with the XPS analysis. Extended X-ray absorption fine structure (EXAFS) analysis revealed that Ga was primarily coordinated with nonmetal atoms, compared to other metals in the literature (Figure 2c). The FTIR spectra showed the presence of Ga-O bonds at 453.40 cm^{-1}; moreover, the absence of noticeable signals of Ga oxide particles in the XRD patterns confirmed that Ga was present in the form of single atoms (Figure S11, Supporting Information). Similarly, Cu was also mainly coordinated with nonmetal atoms (Figure 2d), with no visible CuO crystallization, based on the XRD results. The FTIR spectra showed signals of Cu—O bonds at 578.20 cm^{-1} (Figure S11, Supporting Information), indicating a stable Cu single-atom structure. Additional fitting revealed that Ga adopts a six-coordinate structure with a Ga-O bond length of 1.93 Å (Figure 2e,g; Figures S12a, and S13, and Table S2, Supporting Information), whereas Cu adopts a three-coordinate structure with a Cu-O bond length of 1.96 Å (Figure 2f,h; Figure S12b, and S14, and Table S3, Supporting Information).

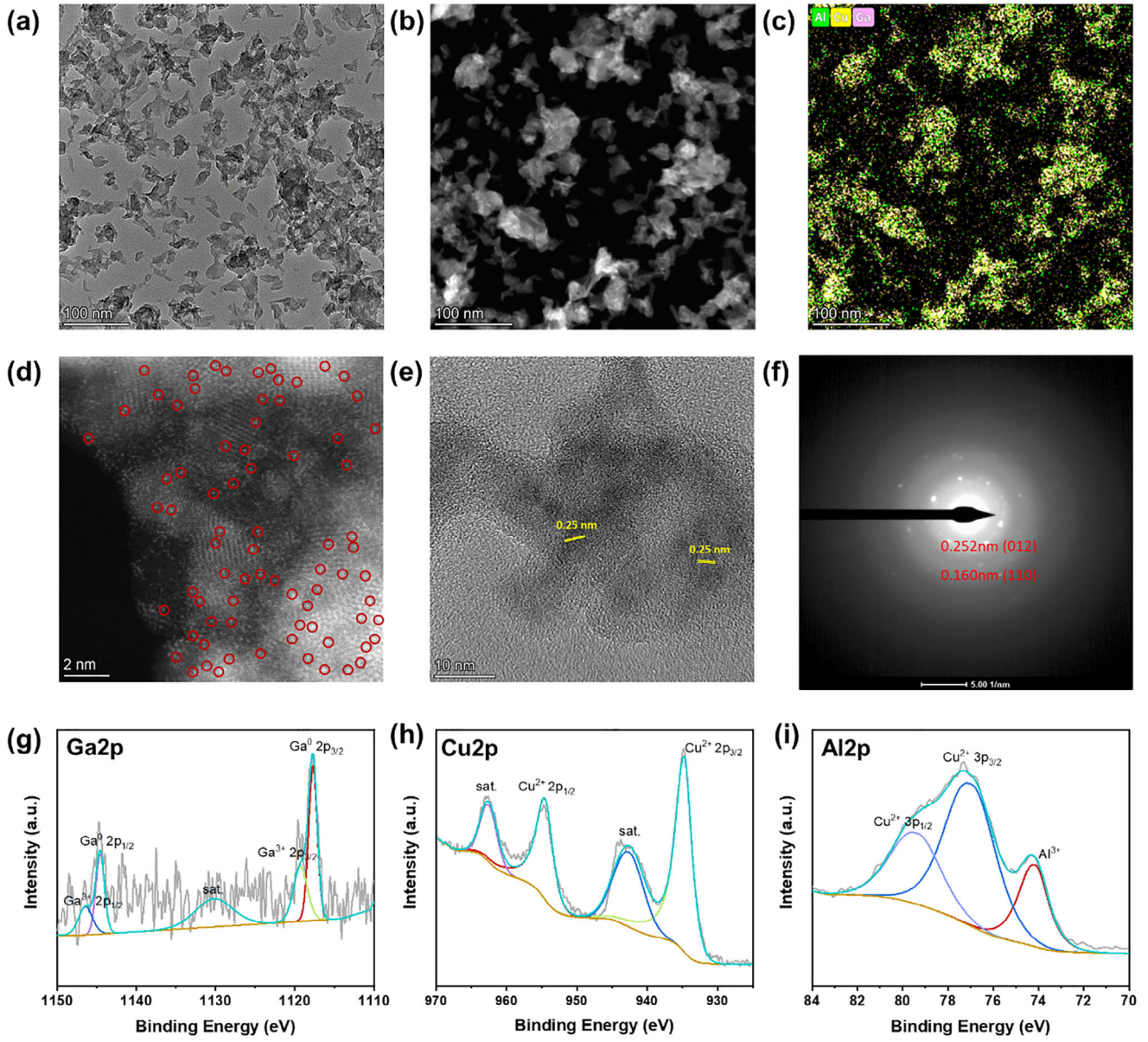

Figure 1. Morphological characterization of GaCu-LDH. a) Bright-field images and b) dark-field images of GaCu-LDH with a particle size of 100 nm. c) EDS elemental mapping images of GaCu-LDH. d) HAADF-STEM, e) TEM, and f) selected-area electron diffraction images of GaCu-LDH. High-resolution g) Ga2p, h) Cu2p, and i) Al2p XPS profiles.

2.2. Enzyme-Like Properties of GaCu-LDH, Ga-LDH, Cu-LDH, and LDH

The enzyme-like catalytic activities of the synthesized GaCu-LDH, Ga-LDH, Cu-LDH, and LDH materials were evaluated, revealing that all four materials exhibited significant peroxidase (POD)-, oxidase (OXD)-, catalase (CAT)-, and glutathione peroxidase (GPx)-like activities. GaCu-LDH exhibited the highest enzyme-like catalytic performance (**Figure** 3a–d; Figure S15, Supporting Information). Additionally, none of the materials exhibited superoxide dismutase (SOD)-like or phenylalanine ammonia-lyase (PPA)-like activity (Figures S16 and S17, Supporting Information). The conditions for the catalytic reaction using the four materials, including the pH, temperature, and enzyme concentration, were further optimized. The optimal pH, temperature, and enzyme concentration for maximizing the POD-like and OXD-like activities were pH 4.0, 35 °C, and 2.5 μM, respectively (Figures S18 and S19, Supporting Information). For the CAT-like and GPx-like activities, the optimal pH levels were 12.0 and 8.0, respectively (Figures S20a and S21a, Supporting Information). Because of the use of the buffer solution detection system and considering practical detection applications, the optimal detection pH was 12. The optimal temperatures were 45 and 35 °C, respectively (Figures S20b and S21b, Supporting Information), and the optimal enzyme concentration was 1.5 μM for both CAT-like and GPx-like activities (Figures S20c and S21c,

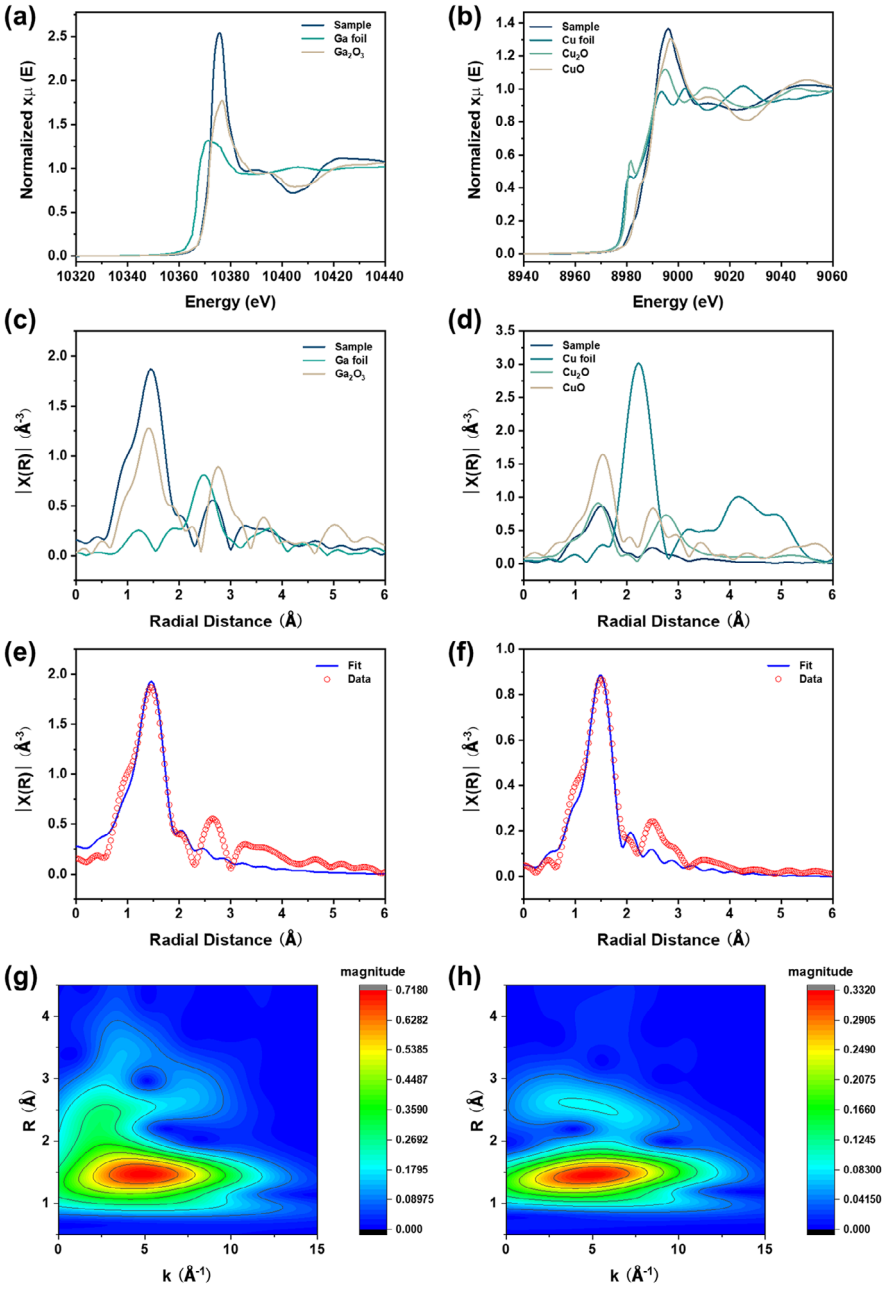

Figure 2. Analysis of atomic structure of GaCu-LDH. a) Comparison of Ga L-edge XANES spectra. b) Comparison of Cu K-edge XANES spectra. c) Comparison of Ga L-edge EXAFS data shown in the k^2-weighted *R*-space. d) Comparison of Cu K-edge EXAFS data shown in the k^2-weighted *R*-space. e) Ga L-edge EXAFS (points) and fit (line) for the sample, shown in the k^2-weighted *R*-space. f) Cu K-edge EXAFS (points) and fit (line) for the sample, shown in the k^2-weighted *R*-space. Wavelet transform of g) Ga and h) Cu.

Supporting Information). Under these optimal conditions, the enzyme-like activity was measured, revealing that the POD-like activity was significantly higher than the enzyme-mimicking activity of the materials for the other three enzymes. Notably, GaCu-LDH exhibited a POD-like activity of 93.62 U/mg (Figure 3e), which is substantially higher than that reported in previous studies.[17,47] The kinetic parameters, including the Michaelis constant (K_m) and maximum reaction rate (v_{max}), indicated that GaCu-LDH displayed stronger substrate affinity in the various enzyme-like catalytic processes, resulting in enhanced enzyme-like catalytic activity (Figures S22–S25, Supporting Information).

To further elucidate the enzyme-like catalytic performance, the generation and quantification of reactive oxygen species (ROS) intermediates, such as hydroxyl radicals (•OH), singlet oxygen ($^1O_2$), and superoxide anions ($O_2^{\cdot-}$), were assessed using terephthalic acid (TA), tryptophan, and *p*-benzoquinone. TA, which selectively recognizes •OH, exhibits fluorescence at 426 nm when excited at 315 nm. Among the tested materials, the

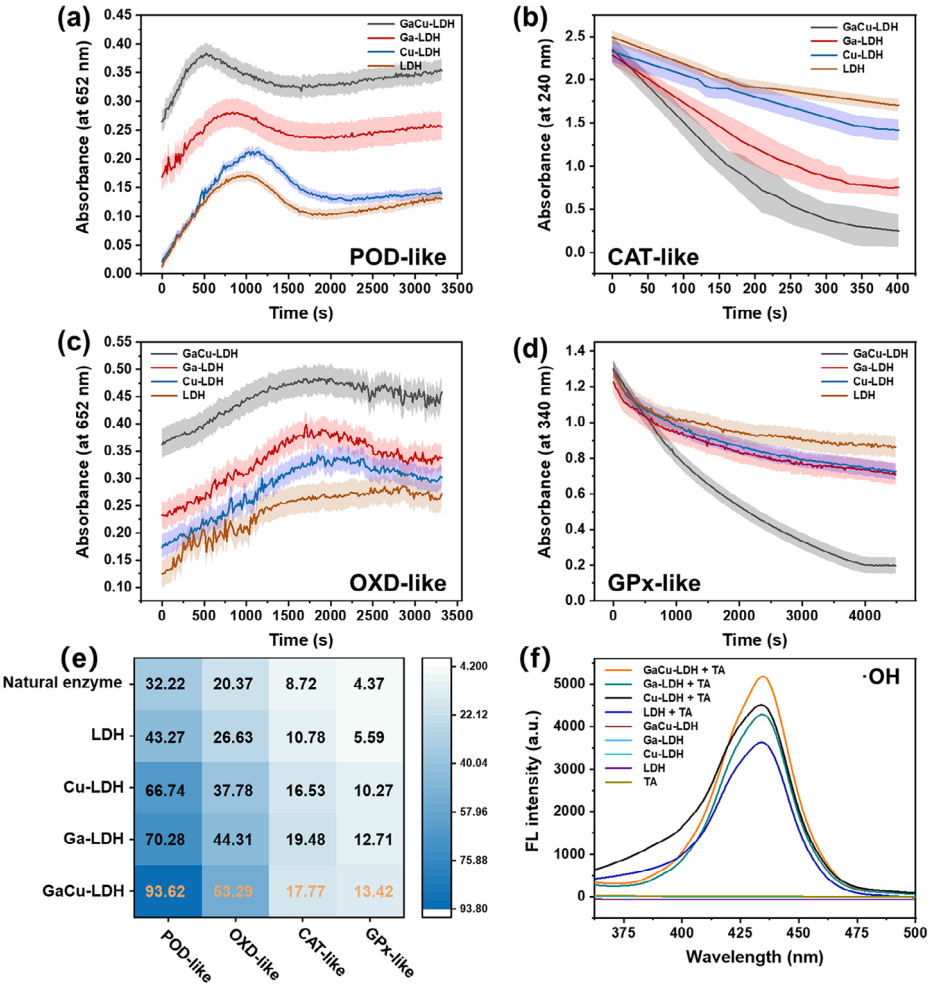

Figure 3. Enzyme-like catalytic properties of GaCu-LDH, Ga-LDH, Cu-LDH, and LDH. a) Reaction-time curves for the POD-like reaction catalyzed by 0.015 g/L GaCu-LDH, Ga-LDH, Cu-LDH, and LDH with 2.0 mM TMB and 0.5 M H_2O_2, respectively. b) Reaction-time curves of the CAT-like reaction catalyzed by 0.015 g/L GaCu-LDH, Ga-LDH, Cu-LDH, and LDH with 0.5 M H_2O_2. c) Reaction-time curves of the OXD-like reaction catalyzed by 0.015 g/L GaCu-LDH, Ga-LDH, Cu- LDH, and LDH with 2.0 mM TMB. d) Reaction-time curves of the GPx-like reaction catalyzed by 0.015 g/L GaCu-LDH, Ga-LDH, Cu-LDH, and LDH with 0.9 mM t-Bu-OOH. e) Comparison of POD-, OXD-, CAT-, and GPx-like catalytic activities. f) Detection of the ·OH intermediate in the POD-like catalytic system.

GaCu-LDH catalytic system exhibited the highest fluorescence intensity (Figure 3f). Tryptophan and *p*-benzoquinone, which serve as $^1O_2$ and $O_2^{\cdot-}$ scavengers, were used to evaluate the effects of these species in the POD-like and OXD-like catalytic systems. As the concentrations of tryptophan and *p*-benzoquinone increased, the absorbance at 652 nm gradually decreased in the catalytic systems of all four materials, with the most significant changes observed in the GaCu-LDH catalytic system (Figures S26 and S27, Supporting Information). These findings indicate that the GaCu-LDH system generated a higher quantity of ROS intermediates, contributing to its enhanced enzyme-like catalytic activity.

2.3. Mechanism of Volatile Amine Recognition by GaCu-LDH

To investigate the interactions of GaCu-LDH, Ga-LDH, Cu-LDH, and LDH with volatile amines, ammonia was initially used as a representative compound and in situ FTIR spectroscopy was employed to determine the adsorption reactions under various temperature conditions. As the temperature increased, a distinct absorption peak appeared at 2425 cm^{-1} for all four systems (GaCu-LDH, Ga-LDH, Cu-LDH, and LDH) at 225 °C, and the peak intensity reached its maximum at 325 °C (**Figure** 4a). This characteristic absorption peak is primarily due to the stretching vibration of the Cu-N bond induced when the Cu in GaCu-LDH forms a complex with NH_3. The peak was significantly stronger for the GaCu-LDH system than for the other three materials (Figure 4b-d), indicating that the adsorption and interaction between ammonia and GaCu-LDH were more robust in the former. When the temperature was further increased to 375 °C, the peak at 2425 cm^{-1} for all four systems began to decline, suggesting the onset of ammonia desorption from the materials. These preliminary findings indicate that ammonia is adsorbed on GaCu-LDH, Ga-LDH, Cu-LDH, and LDH, with the strongest interactions observed in the GaCu-LDH system.

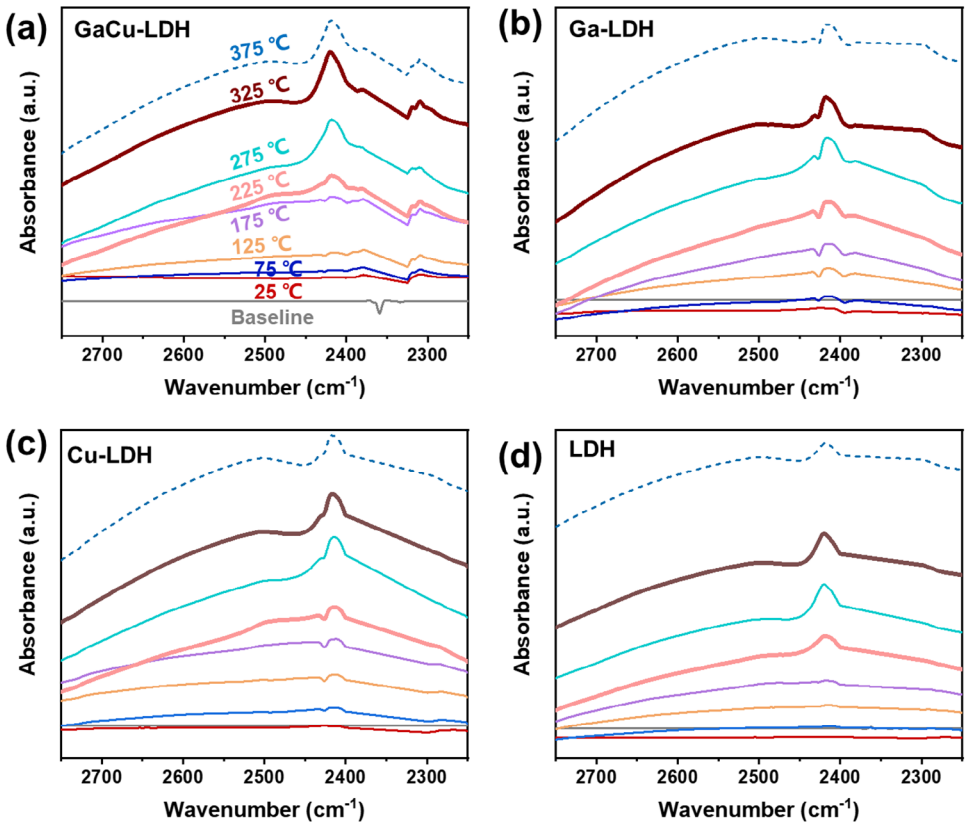

Figure 4. In situ FTIR spectra of a) GaCu-LDH, b) Ga-LDH, c) Cu-LDH, and d) LDH before and after saturation adsorption, and evolution of ammonia desorption during heating from 25 to 375 °C.

Based on the aforementioned findings, the adsorption interactions between GaCu-LDH and eight volatile amines produced during meat spoilage were further investigated. The corresponding structural formulas are shown in Figures S28 and S29 (Supporting Information). The adsorption–binding model presented here represents the optimal binding conformation, where the interaction between the two is the most stable. First, the adsorption energies of GaCu-LDH and the eight volatile amines were calculated. The adsorption energies were ranked as follows: Try (−1.2928 eV) > Phe (−1.2040 eV) > Cad (−1.0616 eV) > Amm (−0.9572 eV) > Put (−0.9515 eV) > His (−0.9040 eV) > Tri (−0.8165 eV) > Dim (−0.7905 eV) (Figure S30 and Table S4, Supporting Information), with lower adsorption energies indicating stronger adsorption capabilities. Preliminary analysis revealed a positive correlation between the adsorption energy and level of unsaturation in the structures of the volatile amines. Based on these results, five volatile amines with strong adsorption capacities were selected for investigating the changes in the bond length, charge distribution, and electron transfer direction following their adsorption on GaCu-LDH. The primary bonding mechanism after adsorption was the formation of Cu-N bonds. The bond lengths were ranked as follows: Try (Cu-N = 1.97918 Å) < Phe (Cu-N = 1.97928 Å) < Amm (Cu-N = 1.98374 Å) < Put (Cu-N = 2.00310 Å) < Cad (Cu-N = 2.01689 Å). Shorter bond lengths indicate stronger binding (Table S5, Supporting Information); moreover, the bond-length trends are consistent with the adsorption energy data, suggesting that stronger adsorption is correlated with shorter Cu-N bond lengths. Electron density difference (EDD) analysis of the charge distribution after adsorption showed that GaCu-LDH experienced significant electron loss, whereas the volatile amines gained electrons (**Figure** 5a–f). The amount of charge and transfer direction of each atom after adsorption and binding were determined using Bader charge calculations. When ammonia interacts with GaCu-LDH, it loses 0.9235 e, which is transferred to the N-H bond that touches GaCu-LDH. The Cu atom on the GaCu-LDH surface loses 0.6987 e, which is also transferred to the N—H bond. Subsequently, the N-H bond loses 0.7548 e, which is transferred to the Ga atom on the GaCu-LDH surface. Finally, the Ga atom loses 0.8174 e, which is transferred to the O atom on the GaCu-LDH surface; this in turn is in contact with both the Ga and Cu atoms. Through this continuous charge-transfer process, the Cu and Ga atoms on the surface of GaCu-LDH ultimately lost 0.6987 and 0.0626 e, respectively, while the N—H bond gained 0.8674 e (Figure 5g). The amount of charge transferred following the adsorption and binding of Cad (Figure S31, Supporting Information), Put (Figure S32, Supporting Information), Try (Figure S33, Supporting Information), and Phe (Figure S34, Supporting Information) to GaCu-LDH was also calculated. The results indicate that synergistic catalysis by the Ga and Cu dual atoms promotes electron transfer in the adsorption and binding of ammonia to GaCu-LDH.

Simultaneously, scanning Kelvin probe microscopy (KPFM) was employed to observe the changes in the morphology, potential, and work function of the GaCu-LDH electrochemical

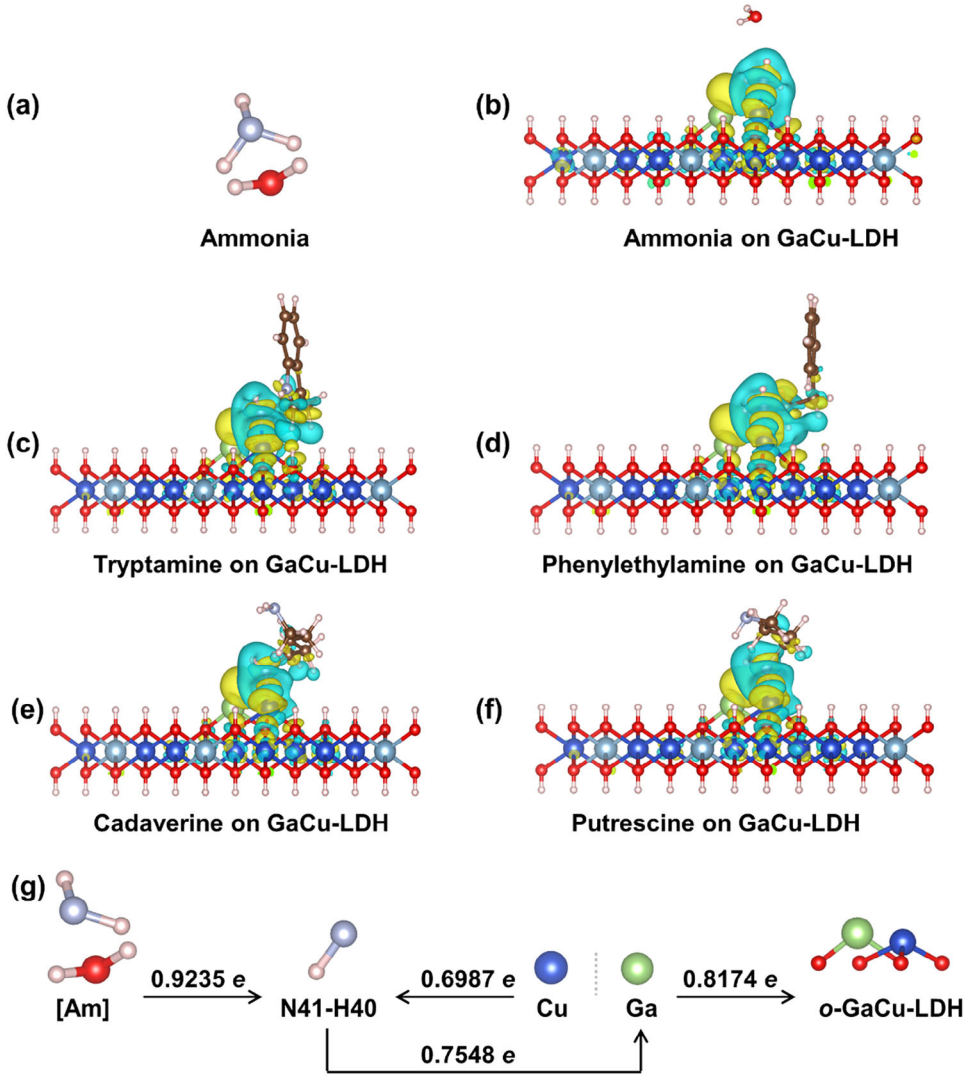

Figure 5. Mechanism by which GaCu-LDH recognizes volatile amines. a) Molecular formula of ammonia. Electron density differences ($\Delta\rho$) for: b) Am, c) Trp, d) Phe, e) Cad, and f) Put-adsorbed GaCu-LDH. g) Schematic of electron transfer in the Am-adsorbed GaCu-LDH system. [Am], *o*-GaCu-LDH, and N41-H40 refer to the atomic electrons in ammonia after removal of the N—H bond, GaCu-LDH metal-peripheral oxygen atom electrons, and GaCu-LDH bonded electrons with ammonia adsorption, respectively. $\Delta\rho$ is defined as $\Delta\rho = \rho - \rho(\text{Ad}) - \rho(\text{GaCu-LDH})$, where ρ, $\rho(\text{Ad})$, and $\rho(\text{GaCu-LDH})$ represent the electron densities in the adsorbed GaCu-LDH configuration, adsorbed species, and GaCu-LDH, respectively. The isovalue of the electron density is set to 0.01 e Å^{-3}. The yellow and cyan regions indicate electron accumulation and depletion, respectively. Cu and Ga eventually lose electrons (0.6987 and 0.0626 e, respectively,) and N41-H40 gains electrons (0.8674 e).

sensing chip before and after interaction with the ammonia solution. This technique was used to further elucidate the sensing mechanisms,[48] and the results are shown in **Figure 6**a,d. The corresponding KPFM images reveal significant morphological changes on the surface of the GaCu-LDH electrochemical sensing chip following the interaction with ammonia (Figure 6b,e). The surface potential shifts from an initial value of 0.198 eV to −0.331 eV (Figure 6c,f), and the work function increases by 0.529 eV (Figure 6g,h). These changes indicate that upon the adsorption of ammonia, the GaCu-LDH electrochemical sensing chip absorbs more electrons from ammonia, resulting in a decrease in its oxidative ability and enhancement of its reductive capacity. This outcome is consistent with that of our previous study.[47]

2.4. Properties of GaCu-LDH Electrochemical Sensor

Owing to its excellent POD-like activity, GaCu-LDH generates electrical signals through redox reactions. When volatile amines were added to the system, the pH of the system increased, which inhibited the redox catalytic action of GaCu-LDH and caused the current signal to change. With an increase in the concentration of volatile amines, the POD-like redox catalytic process of GaCu-LDH was inhibited more significantly, and the current signal decreased considerably. Thus, based on the change in the current signal, the highly sensitive detection of volatile amines was realized. A GaCu-LDH electrochemical sensing chip was developed using screen-printing technology (**Figure 7**a) and was integrated with a portable electrochemical workstation to construct a

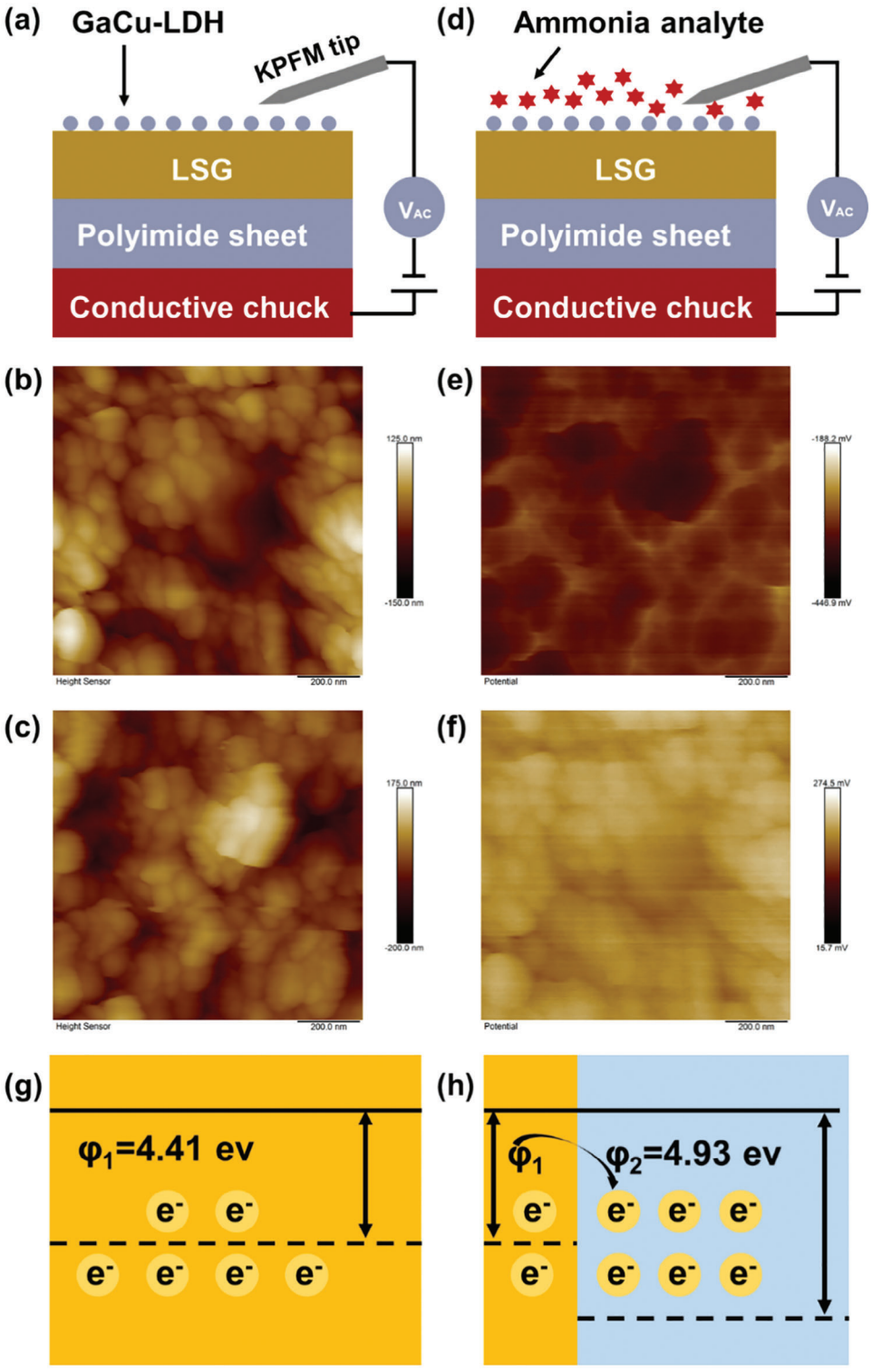

Figure 6. Mechanism of ammonia recognition by the GaCu-LDH electrochemical sensing chip. a) Experimental setup, b) surface, and c) KPFM mapping of the GaCu-LDH electrochemical sensing chip before reaction with ammonia. d) Experimental setup, e) surface, and f) KPFM mapping of the GaCu-LDH electrochemical sensing chip after reaction with ammonia. Work function of the GaCu-LDH electrochemical sensing chip g) before and h) after interaction with the ammonia analyte.

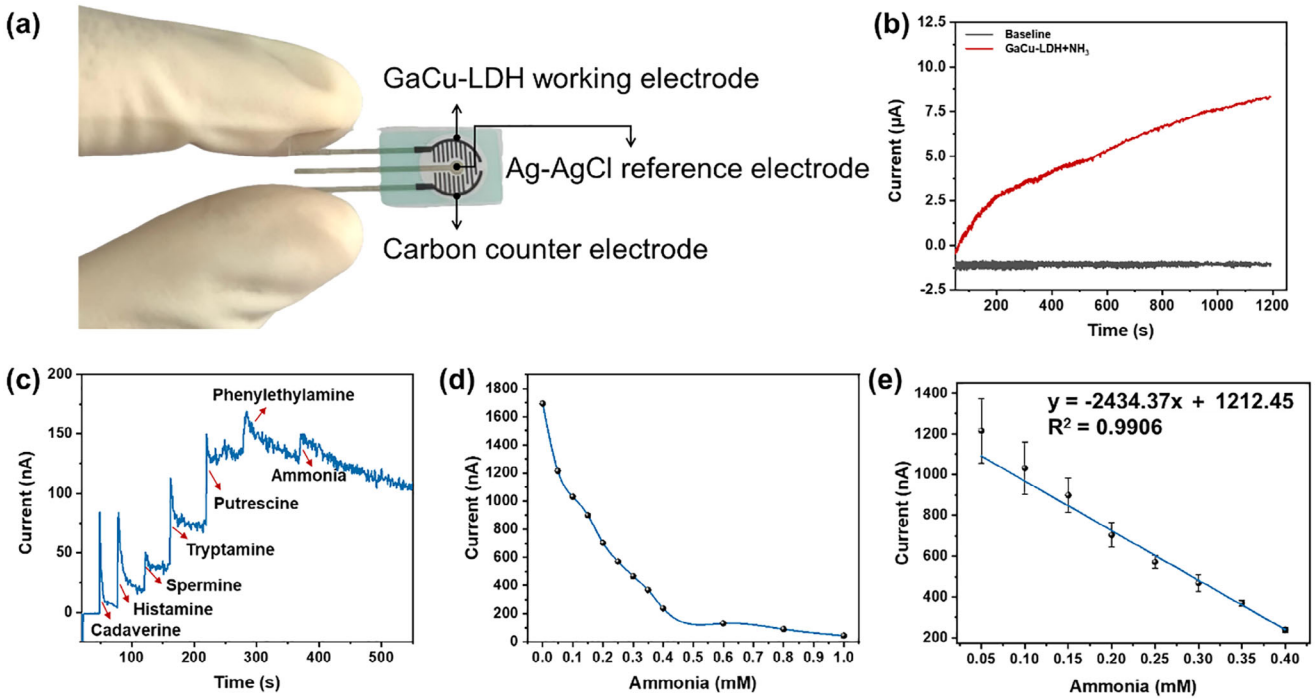

Figure 7. Electrocatalytic response of the GaCu-LDH electrochemical sensing chip toward ammonia. a) Physical schematic of the electrochemical sensing chip. b) *I–t* curves for ammonia on the GaCu-LDH electrochemical sensing chip. c) Selectivity of the GaCu-LDH electrochemical sensing chip toward ammonia. d) Change in current versus ammonia concentration. e) Linear curves for ammonia detection (LOD = $3\sigma/k$, where σ denotes the standard error of the results of 20 blank sample determinations and k is the slope of the linear fit equation).

complete electrochemical detection platform (Figures S35–S37, Supporting Information). First, the performance of the GaCu-LDH electrochemical sensing chip was optimized. Upon exposure to a 0.2 mM ammonia solution, both the *I–t* and cyclic voltammetry (CV) curves of the GaCu-LDH electrochemical sensing chip exhibited significant changes compared with those of the control group (Figure 7b; Figure S38a, Supporting Information), indicating a strong signal response to ammonia. The response time was ≈4 s (Figure S38b, Supporting Information), and the signal intensity increased proportionally with the ammonia concentration (Figure S38c, Supporting Information). Based on these results, the detection conditions, including the pH, potential, and scan rate, were further optimized. The optimal response of the GaCu-LDH electrochemical sensing chip was achieved at a pH of 4.0 (Figure S38d, Supporting Information), potential of 600 mV (Figure S38e, Supporting Information), and scan rate of 200 mV/s (Figure S38f, Supporting Information).

Under the optimal detection conditions, the response of the GaCu-LDH electrochemical sensing chip to various volatile amines was further tested. Although the response of the sensor to different volatile amines differed in magnitude, individual amine compounds were not specifically detected (Figure 7c). Nevertheless, the sensor demonstrated strong anti-interference capabilities against potentially interfering substances (Figure S39, Supporting Information). Based on these results, ammonia was selected as the representative compound for sensitivity testing. In the linear range of 0.05–1 mM, the *I–t* curve displayed a gradual decline in the current, which stabilized after 20 s (Figure 7d; Figure S40a, Supporting Information). The relationship between the ammonia concentration and steady-state currencce week of storage at room temperature, the activity remained above 60% (Figure S40d, Supporting Information).

Therefore, from the perspectives of detection cost and product utilization, the sensor platform developed in this study demonstrates excellent reproducibility, selectivity, and stability.

2.5. Freshness Detection in Pork, Beef, Lamb, and Chicken

Leveraging the excellent performance of the GaCu-LDH electrochemical sensing chip, the content of volatile amines in pork, beef, lamb, and chicken stored at 25 °C and 4 °C was evaluated for various times to assess the freshness of the meat. In this process, supernatants from the meat samples were used to ensure optimal detection results. As the storage time increased, the steady-state current of the GaCu-LDH electrochemical sensing chip decreased (**Figure 8**a,d), whereas the TVB-N content increased (Figure 8b,e). According to the GB5009.228-2016 standard, fresh meat is considered spoiled when its TVB-N content exceeds 15 mg/100 g. At a storage temperature of 25 °C, the spoilage times for pork, beef, lamb, and chicken were 18, 24, 36, and 12 h, respectively (Figure 8b). At 4 °C, the spoilage times for these meats were 5, 7, 7, and 3 d, respectively (Figure 8e). To enable rapid, portable, and intelligent detection, the relationship between the steady-state current and TVB-N content was established. Under storage at 25 °C, the steady-state current exhibited a strong linear correlation with the TVB-N content across different times for pork, beef, lamb, and chicken (R^2 = 0.8521 and R

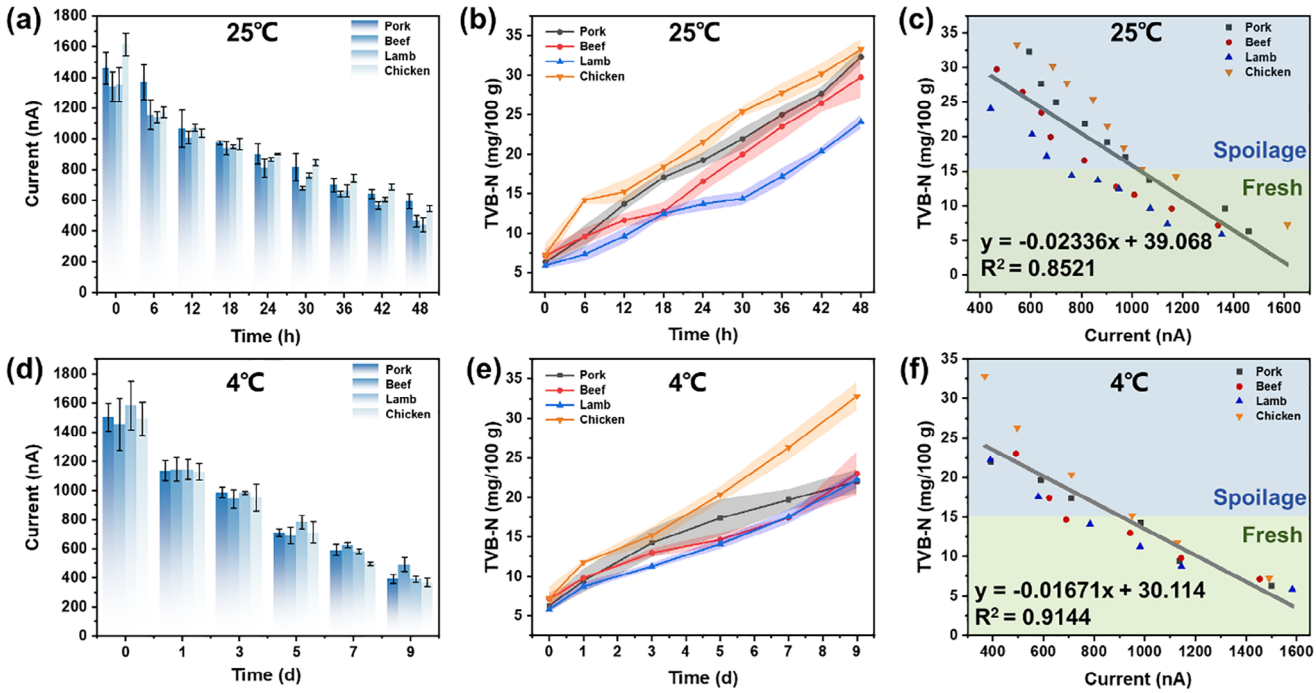

Figure 8. Practical detection of sample freshness. Relationship between current and storage time for pork, beef, lamb, and chicken at a) 25 °C and b) 4 °C. Relationship between TVB-N content and storage time for pork, beef, lamb, and chicken at (b) 25 °C and (e) 4 °C. Relationship between current and TVB-N content in pork, beef, lamb, and chicken at (e) 25 °C and (f) 4 °C.

= 0.9231) (Figure 8c). Similarly, under storage at 4 °C, there was a strong linear relationship between the steady-state current and TVB-N content (R^2 = 0.9144 and R = 0.9562 (Figure 8f). Compared to previous methods, this method demonstrates considerable reliability (Table S6, Supporting Information). These results suggest that the GaCu-LDH electrochemical sensing chip enables the reliable monitoring of the freshness of meat stored at room temperature (25 °C) and under refrigeration (4 °C).

3. Conclusion

A dual GaCu-LDH SAzyme (Ga: 1.31 wt.%, Cu: 4.07 wt.%) was synthesized via coprecipitation using a 2D LDH carrier. The nanozyme demonstrated multiple enzyme-mimicking activities, including POD-like, OXD-like, CAT-like, and GPx-like activity. The incorporation of both Ga and Cu metal atoms overcame the limitations of SAzymes (low catalytic activity, poor stability, and restricted applications) while endowing the LDH structure with superior enzyme-like catalytic properties, thereby enhancing the overall functional performance of the material. The synergistic interaction between Ga and Cu facilitated faster electron transfer on the surface of the material, strengthening its interaction with volatile amines primarily through Cu—N bond formation for recognition and sensing. Based on these results, a rapid and portable electrochemical sensing platform for volatile amine detection was developed using GaCu-LDH, with a linear detection range of 0.05–0.4 mM, detection limit of 5.9 μM, and response time of 4 s. Additionally, the sensor demonstrated reusability for at least four cycles and maintained efficacy for up to 1 week when stored at room temperature. In practical applications, the GaCu-LDH electrochemical sensing platform enabled the rapid and portable detection of freshness for pork, beef, lamb, and chicken stored at 25 and 4 °C, with results comparable to those of standard methods, indicating its reliability and accuracy. Hence, this detection method has significant potential for widespread application in real-world production monitoring and offers promising practical prospects.

Supporting Information

Supporting Information is available from the Wiley Online Library or from the author.

Acknowledgements

This work was financially supported by the Key Program of the National Natural Science Foundation of China (32030086) and National Key Research and Development Program of China (2022YFD2100500).

Conflict of Interest

The authors declare no conflict of interest.

Data Availability Statement

The data that support the findings of this study are available from the corresponding author upon reasonable request.

Keywords

dual single-atom nanozymes, electrochemical sensors, hydrotalcite carrier, meat freshness monitoring

Received: April 30, 2025
Revised: May 30, 2025
Published online:

[1] Y. Liu, Y. He, H. Li, D. Jia, L. Fu, J. Chen, D. Zhang, Y. Wang, *J. Future Foods* **2023**, *4*, 21.
[2] K. V. Kotsanopoulos, I. S. Arvanitoyannis, *Compr. Rev. Food Sci. Food Saf.* **2017**, *196*, 109671.
[3] P. K. Nanda, D. Bhattacharya, J. K. Das, S. Bandyopadhyay, D. Ekhlas, J. M. Lorenzo, P. Dandapat, L. Alessandroni, A. K. Das, M. Gagaoua, *Chemosensors* **2022**, *10*, 322.
[4] Y. Qin, W. Ke, A. Faheem, Y. Ye, Y. Hu, *Food Chem., X* **2023**, *404*, 134581.
[5] J. Zhang, Y. Yang, L. Zeng, J. Wang, *Food Chem.* **2024**, *436*, 137769.
[6] L. Pomponio, J. Ruiz-Carrascal, *J. Sci. Food Agric.* **2017**, *97*, 5211.
[7] R. Dom Nguez, M. Pateiro, M. Gagaoua, F. Barba, W. Zhang, J. Lorenzo, *Antioxidants* **2019**, *8*, 429.
[8] M. Gu, C. Li, Y. Su, L. Chen, S. Li, X. Li, X. Zheng, D. Zhang, *Food Res. Int.* **2023**, *167*, 112684.
[9] S. Dorn-In, L. Führer, M. Gareis, K. Schwaiger, *Food Microbiol.* **2023**, *109*, 104147.
[10] Y. Chen, F. Ma, Y. Wu, S. Tan, A. Niu, W. Qiu, G. Wang, *Food Microbiol.* **2023**, *115*, 104311.
[11] J. Ashiq, U. Saeed, Z. Li, M. H. Nawaz, *J. Food Compos. Anal.* **2024**, *132*, 106295.
[12] B. Okumus, S. Sönmez, S. Moore, D. P. Auvil, G. D. Parks, *Int. J. Hosp. Manag.* **2019**, *81*, 150.
[13] C.-P. Hou, M.-R. Leng, Q.-Y. Yang, J.-F. Xiang, H.-Y. Gong, *Mater. Chem. Front.* **2020**, *4*, 1192.
[14] X. Tang, Z. Yu, *Int. J. Food Prop.* **2020**, *23*, 297.
[15] S. Chen, S. Brahma, J. Mackay, C. Cao, B. Aliakbarian, *J. Food Sci.* **2020**, *85*, 517.
[16] A. E.-D. A. Bekhit, B. W. B. Holman, S. G. Giteru, D. L. Hopkins, *Trends Food Sci. Technol.* **2021**, *109*, 280.
[17] G. Song, Z. Zhang, M.-L. Fauconnier, C. Li, L. Chen, X. Zheng, D. Zhang, *Nano Today* **2023**, *53*, 102025.
[18] M. Gu, C. Li, L. Chen, S. Li, N. Xiao, D. Zhang, X. Zheng, *Food Chem.* **2023**, *424*, 136341.
[19] Y. Salinas, J. V. Ros-Lis, J.-L. Vivancos, R. Martínez-Manez, M. D. Marcos, S. Aucejo, N. Herranz, I. Lorente, *Analyst* **2012**, *137*, 3635.
[20] M. A. Munir, K. H. Badri, *J. Anal. Methods Chem.* **2020**, 5814389.
[21] N. Ding, S. Dong, Y. Zhang, D. Lu, J. Lin, Q. Zhao, X. Shi, *Sens. Actuators B, Chem.* **2022**, *363*, 131811.
[22] S. Sutthasupa, C. Padungkit, S. Suriyong, *Food Chem.* **2021**, *362*, 130151.
[23] Y. Congchao, H. Tien, R. Victor, Y. Jerry, W. Lin, *Anal. Methods* **2023**, *35*, 4427.
[24] Y. Yuan, D. Zhang, X. Huang, Y. Yin, H. Yu, X. Li, *Food Anal. Methods* **2022**, *15*, 2691.
[25] Q. Ouyang, M. Lizareef, Z. Quanshengguo, L. Huanhuan, *Microchem. J.* **2020**, *157*, 105020.
[26] N. Wang, N. Zhang, T. Wang, F. Liu, X. Wang, X. Yan, C. Wang, X. Liu, P. Sun, G. Lu, *Sens. Actuators B, Chem.* **2022**, *350*, 130854.
[27] T. Yamamoto, J. N. Taylor, S. Koseki, K. Koyama, *J. Microbiol. Methods* **2021**, *190*, 106326.
[28] L. Chen, H. Jiang, M. Zheng, Z. Li, N. Li, S. Zhao, X. Liu, *J. Hazard. Mater.* **2022**, *434*, 128868.
[29] Y.-X. Sun, Z.-J. Yan, W.-X. Liu, X.-M. Chen, M.-H. Ding, L.-L. Tang, F. Zeng, *Molecules* **2024**, *29*, 1818.
[30] Y. Tan, H. Yi, X. T. Y. G. L. W. Z. K. Zhao, *J. Clean. Prod.* **2024**, *436*, 140635.
[31] Z. Guo, J. Hong, N. Song, M. Liang, *Acc. Mater. Res.* **2024**, *5*, 347.
[32] E. M. Hamed, F. M. Fung, *ACS Sens.* **2024**, *9*, 3840.
[33] H. Zhang, X. F. Lu, Z.-P. Wu, X. W. D. Lou, *ACS Cent. Sci.* **2020**, *6*, 1288.
[34] W. Zhang, Y. Zhao, W. Huang, T. Huang, B. Wu, *Coord. Chem. Rev.* **2024**, *515*, 215952.
[35] F. Meng, P. Zhu, L. Yang, *Chem. Eng. J.* **2023**, *452*, 139411.
[36] H. Hu, Y. Zhao, Y. Zhang, J. Xi, J. Xiao, S. Cao, *Top. Curr. Chem.* **2023**, *381*, 24.
[37] S. Kumari, A. Sharma, S. Kumar, A. Thakur, R. Thakur, S. K. Bhatia, A. K. Sharma, *Chemosphere* **2022**, *306*, 135464.
[38] M. Xu, M. Wei, *Adv. Funct. Mater.* **2018**, *28*, 1802943.
[39] G. Fan, F. Li, D. Evans, X. Duan, *Chem. Soc. Rev.* **2015**, *45*, 7040.
[40] Q. Liu, J. Ma, K. Wang, T. Feng, M. Peng, Z. Yao, C. Fan, S. Komarneni, *Ceram. Int.* **2017**, *43*, 5751.
[41] R. Li, Y. Li, X. Jia, J. Yang, X. Miao, D. Shao, L. Feng, S. Wang, J. Wu, H. Song, *Ceram. Int.* **2023**, *49*, 14635.
[42] Q. Wang, D. O'Hare, *Chem. Rev.* **2012**, *112*, 4124.
[43] J. Shen, J. Chen, Y. Qian, X. Wang, D. Wang, H. Pan, Y. Wang, *Adv. Mater.* **2024**, *36*, 2313406.
[44] W. Ying, W. Yong, S. W. Kwok-Yin, *Nanoscale* **2023**, *15*, 18173.
[45] Q. Chen, Y. Liu, Y. Lu, Y. Hou, X. Zhang, W. Shi, Y. Huang, *J. Hazard. Mater.* **2022**, *422*, 126929.
[46] K. Wang, Q. Hong, C. Zhu, Y. Xu, W. Li, Y. Wang, W. Chen, X. Gu, X. Chen, Y. Fang, Y. Shen, S. Liu, Y. Zhang, *Nature Commun* **2024**, *15*, 5705.
[47] G. Song, X. Zheng, Z. Zhang, M.-L. Fauconnier, C. Li, L. Chen, D. Zhang, *Chem. Eng. J.* **2024**, *500*, 156835.
[48] G. Tostado-Blazquez, S. S. Shetty, S. Yuvaraja, J. L. Cerrillo, V. Mani, K. N. Salama, *Small Sci* **2024**, *4*, 2300259.